

DRAFT VERSION APRIL 23, 2024

Typeset using L^AT_EX **modern** style in AASTeX63

Plasma Waves near the Electron Cyclotron Frequency in the near-Sun Solar Wind

DAVID M. MALASPINA,^{1,2} JASPER HALEKAS,³ LAURA BERČIČ,^{4,5} DAVIN LARSON,⁶
 PHYLLIS WHITTLESEY,⁶ STUART D. BALE,^{6,7} JOHN W. BONNELL,⁶
 THIERRY DUDOK DE WIT,⁸ ROBERT E. ERGUN,^{1,2} GREGORY HOWES,³
 KEITH GOETZ,⁹ KATHERINE GOODRICH,⁶ PETER R. HARVEY,⁶
 ROBERT J. MACDOWALL,¹⁰ MARC PULUPA,⁶ ANTHONY W. CASE,¹¹
 JUSTIN C. KASPER,¹² KELLY E. KORRECK,¹¹ ROBERTO LIVI,⁶
 MICHAEL L. STEVENS,¹¹

¹*Astrophysical and Planetary Sciences Department, University of Colorado, Boulder, CO, USA*

²*Laboratory for Atmospheric and Space Physics, University of Colorado, Boulder, CO, USA*

³*University of Iowa, Iowa City, IA, USA*

⁴*LESIA, Observatoire de Paris, PSL Research University, CNRS, Meudon, France*

⁵*Physics and Astronomy Department, University of Florence, Italy*

⁶*Space Sciences Laboratory, University of California, Berkeley, CA, USA*

⁷*Physics Department, University of California, Berkeley, CA, USA*

⁸*LPC2E, CNRS, and University of Orléans, Orléans, France*

⁹*School of Physics and Astronomy, University of Minnesota, Minneapolis, MN, USA*

¹⁰*NASA Goddard Space Flight Center, Greenbelt, MD, USA*

¹¹*Harvard-Smithsonian Center for Astrophysics, Cambridge, MA, USA*

¹²*University of Michigan, Ann Arbor, MI, USA*

(Received September 10, 2019; Revised –; Accepted –)

Submitted to ApJ

ABSTRACT

Corresponding author: David M. Malaspina

David.Malaspina@colorado.edu

Data from the first two orbits of the Sun by Parker Solar Probe reveal that the solar wind sunward of 50 solar radii is replete with plasma waves and instabilities. One of the most prominent plasma wave power enhancements in this region appears near the electron cyclotron frequency (f_{ce}). Most of this wave power is concentrated in electric field fluctuations near $0.7 f_{ce}$ and f_{ce} , with strong harmonics of both frequencies extending above f_{ce} . At least two distinct, often concurrent, wave modes are observed, preliminarily identified as electrostatic whistler-mode waves and electron Bernstein waves. Wave intervals range in duration from a few seconds to hours. Both the amplitudes and number of detections of these near- f_{ce} waves increase significantly with decreasing distance to the Sun, suggesting that they play an important role in the evolution of electron populations in the near-Sun solar wind. Correlations are found between the detection of these waves and properties of solar wind electron populations, including electron core drift, implying that these waves play a role in regulating the heat flux carried by solar wind electrons. Observation of these near- f_{ce} waves is found to be strongly correlated with near-radial solar wind magnetic field configurations with low levels of magnetic turbulence. A scenario for the growth of these waves is presented which implies that regions of low-turbulence near-radial magnetic field are a prominent feature of solar wind structure near the Sun.

Keywords: Solar wind – wave-particle interactions – electrons populations – inner heliosphere

1. INTRODUCTION

Sunward of ~ 50 solar radii (R_S), Parker Solar Probe detects intervals of strong wave power near the electron cyclotron frequency (f_{ce}). These intervals range in duration from a few seconds to several hours. The observed waves are electrostatic up to the sensitivity of the FIELDS instrumentation (no measurable signature in the search coil magnetometer). Most of the wave power is concentrated at and below the

electron cyclotron frequency (f_{ce}), and these waves often show strong harmonics. At least two distinct concurrent wave modes are preliminarily identified as electrostatic whistler-mode waves and electron Bernstein waves.

The amplitude and number of detections of these near- f_{ce} waves increases significantly as Parker Solar Probe approaches the Sun, suggesting that they play a role in the evolution of electron populations in the near-Sun plasma environment. Correlations are observed between the detection of these waves and properties of solar wind electrons, which are composed of a core, halo, and strahl (the population of electrons escaping the solar corona) (Montgomery et al. 1968; Feldman et al. 1975; Pilipp et al. 1987; Maksimovic et al. 2005). These correlations suggest that these waves play a role in regulating the solar heat flux carried by electrons. Finally, the detection of these waves is found to be strongly correlated with the presence of low-turbulence radial solar wind magnetic fields.

Previous observations of plasma waves in the solar wind near f_{ce} focused on whistler-mode waves. These waves were reported in three primary contexts: (i) associated with solar wind plasma boundaries such as shocks (e.g. (Wilson et al. 2009; Ramírez Vélez et al. 2012) and references therein) and stream interaction regions (Beinroth & Neubauer 1981; Lin et al. 1998; Lengyel-Frey et al. 1996; Breneman et al. 2010), (ii) associated with the turbulent cascade of magnetic field fluctuations (e.g. (Lengyel-Frey et al. 1996; Bruno & Carbone 2013; Narita et al. 2016) and references therein), and (iii) present in the free solar wind (Zhang et al. 1998; Lacombe et al. 2014; Stansby et al. 2016; Tong et al. 2019).

Waves in context types i and iii are narrowband (clear sinusoidal waveforms in time-domain data), whereas the waves in context type ii are a superposition of waves, without clear sinusoidal waveforms. We do not elaborate further on the whistler-mode waves in context types i or ii, because the near- f_{ce} waves observed by Solar Probe

are not limited to association with shocks or stream interaction regions, and they are narrowband rather than broadband.

Whistler-mode waves in the free solar wind are often thought to be generated by electron temperature anisotropy and/or heat flux instabilities (those involving a beaming component) (Gary et al. 2005; Shaaban et al. 2018). Many numerical studies have focused on this issue (e.g. (Vocks et al. 2005; Saito & Gary 2007; Seough et al. 2015) and references therein), and data analyses of the radial evolution of solar wind electron distribution functions are frequently interpreted in terms of whistler-mode waves driving electron scattering (Walsh et al. 2013; Graham et al. 2017; Berčič et al. 2019). Further, observed correlations between whistler-mode wave detection and properties of electron distribution functions have been reported (Kajdič et al. 2016; Stansby et al. 2016; Tong et al. 2019).

The near- f_{ce} wave observations from Parker Solar Probe presented here are distinct from the vast majority of those reported in these prior studies in several regards: (i) the wave frequencies are considerably higher, centered on $0.7 f_{ce}$ or f_{ce} in Parker Solar Probe data, compared to $0.1 < f/f_{ce} < 0.3$ reported in prior studies (Lengyel-Frey et al. 1996; Lin et al. 1998; Moullard et al. 2001; Lacombe et al. 2014; Kajdič et al. 2016; Stansby et al. 2016; Tong et al. 2019), (ii) the waves are electrostatic up to the sensitivity of the FIELDS data, whereas most prior studies identified whistler-mode waves using exclusively magnetic field data (Beinroth & Neubauer 1981; Lacombe et al. 2014; Kajdič et al. 2016; Tong et al. 2019), (iii) the waves observed by Parker Solar Probe are both narrow band and frequently observed, observed up to 30% of the time when magnetic field conditions favorable to wave growth exist (prior studies of non-turbulence whistler-mode waves show much lower detection rates (e.g. (Lacombe et al. 2014; Tong et al. 2019))), and (iv) the near- f_{ce} waves observed by Parker Solar Probe often include electron Bernstein modes, which have previously been reported

in the solar wind only near shocks (Wilson et al. 2010) or in conjunction with the AMPTE Li ion release (Baumgaertel & Sauer 1989).

In addition to the waves described here, Parker Solar Probe does observe electromagnetic whistler-mode waves near $0.1 f_{ce}$ (simultaneously observed signatures in both electric and magnetic field data with right-handed near-circular polarization). However, these lower frequency waves are not nearly as prevalent as the waves near f_{ce} do not show the strong correlations with respect to ambient magnetic field properties described here.

A full understanding of the origins of the near- f_{ce} waves in the near-Sun solar wind, their potential importance to the evolution of solar wind electrons, and the information they carry about the large-scale structure of the solar wind will require considerable study. Here we begin that process by reporting the existence of these waves, their observed properties, and correlations with solar wind conditions.

2. DATA SET AND PROCESSING

Parker Solar Probe is a NASA mission designed to explore the near-Sun plasma environment (Fox et al. 2016). Its prime mission consists of 24 orbits of the Sun, with progressively decreasing perihelion distances. The first two orbits, data from which are reported here, have a perihelion distance of 35.68 solar radii (R_S). The solar 'encounter' where all Parker Solar Probe instruments operate at their nominal cadences begins at $\sim 55 R_S$, providing radial coverage over $\sim 20 R_S$ for the first two orbits.

The FIELDS instrument (Bale et al. 2016) measures in-situ electric fields from DC to ~ 20 MHz and in-situ magnetic fields from DC to ~ 1 MHz. Electric fields are measured using five sensors. Four of these are 2m whip antennas located in the plane of the spacecraft heat shield and extending outward from the heat shield. Opposing antennas are 180° apart and the two antenna pairs are 5° from orthogonal with each other. The differential voltage measurements made by these sensor pairs are

designated V_{12} ($= V_1 - V_2$) and V_{34} ($= V_3 - V_4$). The fifth sensor is a ~ 21 cm antenna located on the magnetometer boom, in the umbra of the heat shield, 3.08 m from the spacecraft bus. Magnetic fields are measured by a fluxgate magnetometer (DC to ~ 146.5 S/s on three orthogonal axes) and a search coil magnetometer ($\sim 10Hz$ to ~ 20 kHz on three orthogonal axes, $\sim 10kHz$ to ~ 1 MHz on one axis). All magnetic field sensors are located along the 3.5 m magnetometer boom.

This study utilizes power spectra calculated on-board by the FIELDS Digital Fields Board (DFB) (Malaspina et al. 2016). During the first two solar encounters, the reported AC power spectra are the mean of 16 individual power spectra calculated during the first 1/8 of each New York second (NYs = $2^{17} / 150,000 \approx 0.874$ s (Bale et al. 2016)). AC power spectra are calculated for 4 channels. For the first solar encounter, these channels were V_{12} and the three low-frequency *SCM* axes. For the second solar encounter, these channels were V_{12} , V_{34} , V_5 , and the single-axis high frequency *SCM* winding. For the first two encounters, the power spectral data were configured have 56 pseudo-logarithmically spaced frequency bins.

This study utilizes data from the SWEAP instrument suite (Kasper et al. 2016), including proton moments from the sunward-facing SPC Faraday cup and electron distribution function data from the SPANe electron analyzers on the ram and anti-ram faces of the Parker Solar Probe spacecraft.

3. ANALYSIS

Figure 1 shows an example interval of near- f_{ce} waves recorded on April 4, 2019. The interval lasts ~ 30 min. Figures 1a, 1b, and 1c show AC power spectra for V_{12} , V_{34} , and V_5 . The local value of f_{ce} is indicated by a white line in each Figure. Figure 1d shows the three components of the DC-coupled solar wind magnetic field in RTN coordinates. These data were recorded near the second perihelion ($\sim 36 R_S$). The strongest wave power is generally observed at $\sim 0.7 f_{ce}$ and significant harmonics are observed with amplitudes well above known instrumental response harmonics

(Malaspina et al. 2016). During sub-intervals (e.g. near 06:39 or 06:24:00 UTC), the strongest wave power occurs near $\sim 1.0 f_{ce}$, with significant harmonics. Because this can be difficult to discern in Figures 1a - 1d given the line indicating f_{ce} , Figures 1e - 1h show spectrograms and magnetic field data in the same format as Figures 1a - 1d, but focused on a short time interval from 06:39 to 06:41 UTC. Black arrows indicate f_{ce} during this interval. Wave power at f_{ce} and its harmonic is present.

The ambient solar wind magnetic field is disturbed prior to and after the wave interval, but is significantly less disturbed during the wave interval. The solar wind magnetic field is also close to radial during the wave interval ($\sim 10^\circ$ between the magnetic field vector and the direction radially outward from the Sun).

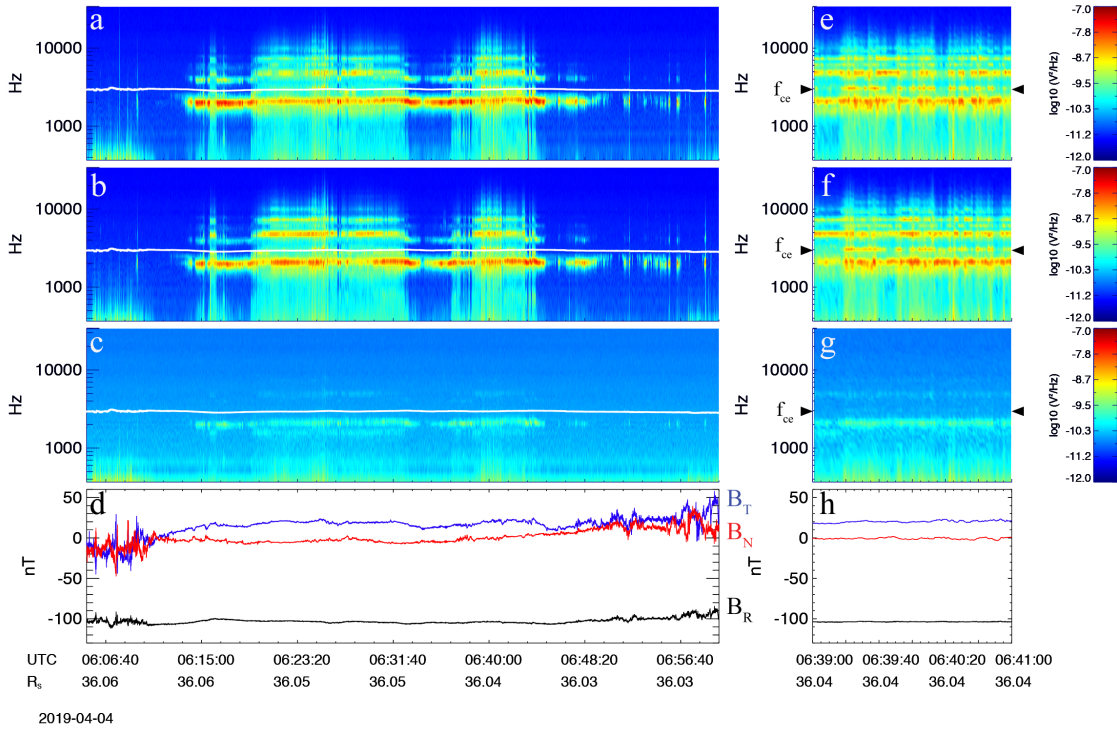


Figure 1. Example of near- f_{ce} waves in the near-Sun solar wind. (a,b,c) Spectrograms of V_{12} and V_{34} differential voltage measurements and the V_5 single-ended voltage measurement, respectively. Thick white lines indicate the local electron cyclotron frequency. (d) Ambient magnetic field vector in RTN coordinates. (e,f,g,h) Spectrograms and magnetic field from 06:39 to 06:41 UTC, in the same format as (a,b,c,d). Black arrows indicate f_{ce} during these two seconds.

To examine the degree to which near- f_{ce} waves are observed in association with near-radial solar wind magnetic field, an automated detection algorithm was applied to solar encounter 1 and 2 data to identify wave intervals. First, each power spectra was converted to dB relative to background, where the background for each spectrum is defined as the median wave power at each frequency during the day when the observation was made. Next, all peaks in each power spectra were identified using first and second derivatives (in the frequency dimension) of the power spectral data. Power spectra where the largest peak was less than 8 dB above the noise were excluded from consideration. Power spectra where the largest peak was less than $0.5 f_{ce}$ or more than $1.1 f_{ce}$ were also excluded from consideration. Finally, a peak was identified as a potential near- f_{ce} wave when the amplitude of the peak was at least 8 dB larger than the power of the first spectral point on either side of the peak where the derivative of the power spectra (in the frequency dimension) changed sign. This algorithm was applied to the V_{12} onboard AC spectral data only, as those data are available for both the first and second perihelion passes. In all, 6.7 hours ($\sim 27,000$ individual wave spectra) of data were found to contain near- f_{ce} waves during solar encounter 1 and 9.12 hours ($\sim 37,000$ individual wave spectra) during solar encounter 2.

For each spectra identified as containing near- f_{ce} waves, the angle between the solar wind magnetic field vector and the radial direction (θ_{Br}) was calculated as the mean of the angle between the solar wind magnetic field vector and the radial direction over the NYs corresponding to each power spectral measurement. The sense of the radial field (sunward or anti-sunward) was not retained, such that the range of θ_{Br} is $0^\circ < \theta_{Br} < 90^\circ$.

Figure 2 compares the distributions of θ_{Br} for times when near- f_{ce} waves were detected (black curves) and all solar wind (blue curves). To enable comparisons, all distributions are normalized to their maximum value. Statistics for each solar encounter are shown as two columns (Figures 2a,2b,2c, and Figures 2d,2e,2f). The

data are divided into 5 R_S segments. In each case, the vast majority of near- f_{ce} waves are detected for $\theta_{Br} < 25^\circ$. Examining the few waves identified as near- f_{ce} waves where $\theta_{Br} > 25^\circ$ reveals that these are low-amplitude, isolated (to a single spectra) waves without harmonic signatures. From these data, we conclude that near-radial magnetic field is a necessary environmental condition for near- f_{ce} wave growth.

The distributions with wave detections (black curves) peak between $\sim 10^\circ$ and $\sim 15^\circ$, which approximately corresponds to the Parker spiral magnetic field deflection angle expected for undisturbed radially propagating solar wind by the time it reaches 35 and 55 solar radii, respectively (assuming 400 km/s solar wind).

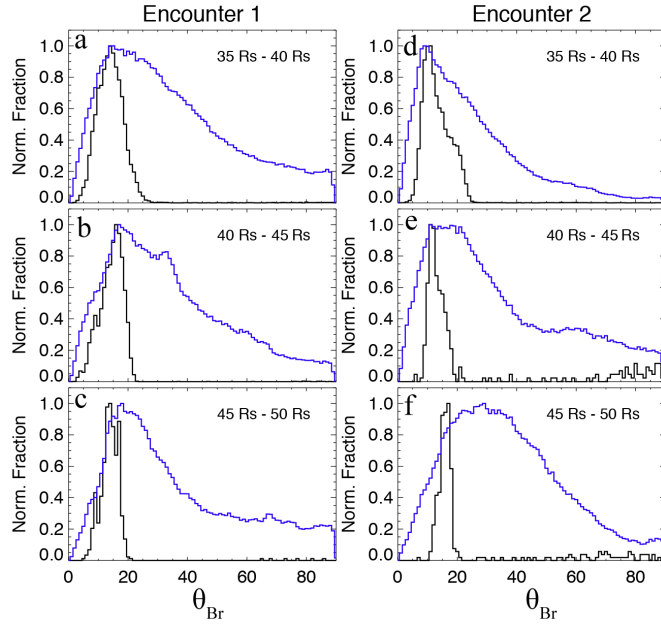


Figure 2. Histograms of θ_{Br} , the angle between the solar wind magnetic field vector and the radial direction. Data for when near- f_{ce} waves were detected are indicated by black curves. Data for all times are indicated by blue curves. All curves are normalized to their maximum value. (a,b,c) Histograms of θ_{Br} for solar Encounter 1, for the three indicated radial distance ranges. (c,d,e) Same as (a,b,c), but for solar Encounter 2.

Figure 3 examines the variation in detection of near- f_{ce} waves with radial distance to the Sun. Figures 3a and 3d show the number of hours where $\theta_{Br} < 25^\circ$ as a function

of distance to perihelion (with 1 R_S bins) for solar encounters 1 and 2, respectively. Figures 3b and 3e show the number of hours when near- f_{ce} waves were detected. Figures 3c and 3f show the fraction of the solar wind magnetic field near-radial time when near- f_{ce} waves were detected. These data demonstrate that, when the magnetic field orientation is favorable for these waves to grow ($\theta_{Br} < 25^\circ$), they are observed between 10% and 30% of the time.

The radial profile of radial magnetic field observation is, to first order, symmetric with respect to the inbound and outbound motion of Parker Solar Probe for both solar encounters (Figures 3a, 3d). On encounter 2, the observation of near- f_{ce} waves is likewise symmetric to first order (Figures 3e, 3f). On encounter 1, the observation of near- f_{ce} waves was not radially symmetric (Figures 3b, 3c). From these data, we conclude that near-radial magnetic field is a necessary, but not sufficient, environmental condition for near- f_{ce} wave growth.

Figure 4 examines the variation in amplitude and frequency of near- f_{ce} waves with radial distance to the Sun. Figure 4a shows a two dimensional histogram of near- f_{ce} wave detections as a function of V_{12} amplitude (in dB, of the largest spectral peak for each spectra) and distance, for solar encounter 1. Figure 4c shows a similar plot for solar encounter 2. For both encounters, the observation rate of higher amplitude near- f_{ce} waves increases toward perihelion, demonstrating that the waves become stronger and more frequent closer to the Sun. The inbound / outbound symmetry in these figures follows that in Figure 3.

Figure 4b shows a two dimensional histogram of near- f_{ce} wave detections as a function of wave frequency (frequency of the largest amplitude spectral peak for a given spectra) and distance, for solar encounter 1. Figure 4d shows a similar plot for encounter 2. These data demonstrate that the presence of two wave modes inferred from case studies also appears in statistical analysis of the data. Particularly in solar

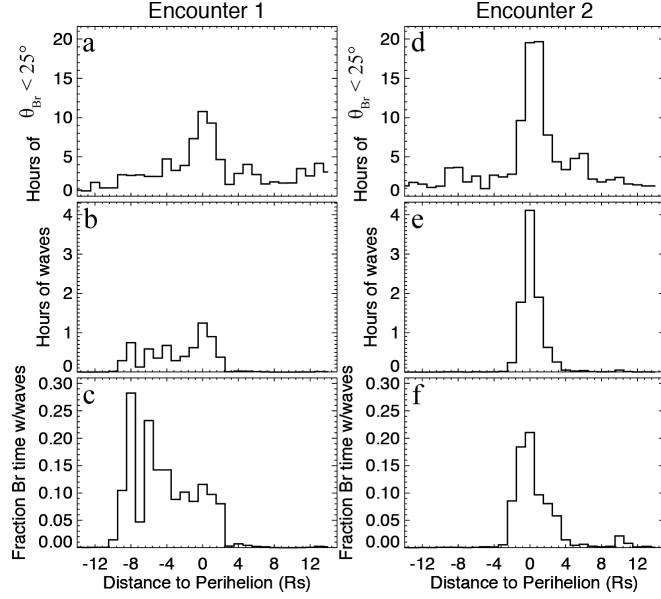


Figure 3. Histograms of θ_{Br} and near- f_{ce} wave detections as a function of distance to perihelion. (a,d) Histogram of hours of data where $\theta_{Br} < 25^\circ$ for. (b,e) Histogram of hours of data where near- f_{ce} waves are identified. (c,f) Histogram of the fraction of the solar wind magnetic field radial time when near- f_{ce} waves were detected. (a,b,c) show data for solar encounter 1 and (d,e,f) for encounter 2.

encounter 1, two distinct populations can be discerned, one with $0.6f_{ce} < f < 0.8f_{ce}$ and one with $0.9f_{ce} < f < 1.1f_{ce}$.

Figure 5 shows an interval of near- f_{ce} waves along with proton moments as determined by SPC. Figure 5a, 5b, 5c, 5d, and 5e show, respectively, the V_{12} wave spectra, the DC-coupled magnetic field, solar wind velocity (spacecraft velocity removed), solar wind density, and proton temperature. The period of wave activity is bracketed by distinct changes in solar wind conditions. While these specific conditions (low density, faster solar wind speed) are not found to be broadly correlated with near- f_{ce} wave detection, these data do demonstrate that the solar wind associated with the near- f_{ce} waves is distinctly different from the surrounding wind.

With regard to 5e, it is important to note that SPC determines proton temperature in the sunward direction, such that the observed temperature variation may reflect a transition between measuring the temperature parallel to the background mag-

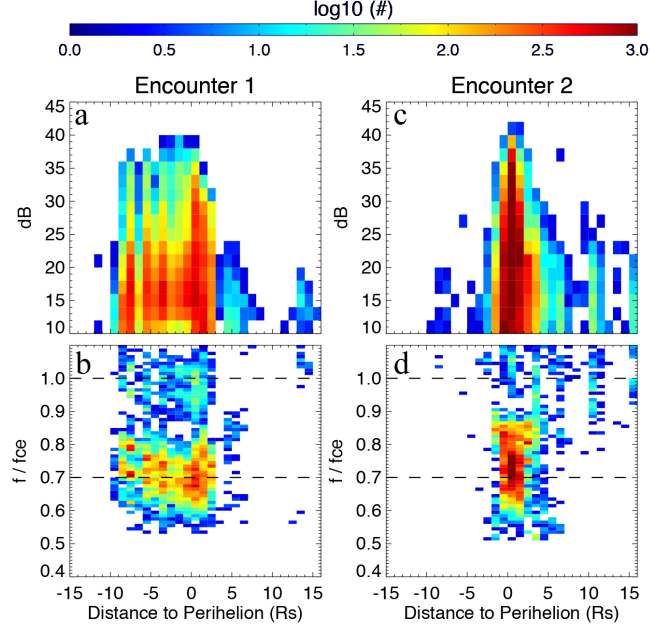


Figure 4. Two dimensional histograms showing the number of near- f_{ce} waves detected as a function of amplitude (in dB) or frequency (normalized to f_{ce}) and distance to perihelion. (a,b) show data for solar encounter 1. (c,d) show data for solar encounter 2.

netic field (radial field) and measuring a combination of parallel and perpendicular temperatures (non-radial field).

To understand this difference in solar wind in a quantitative way, Figure 6 explores the relationship between solar wind with low-amplitude magnetic fluctuations (‘quiet’ solar wind) and near- f_{ce} waves. Figure 6a shows a two dimensional histogram of wave detection rate versus magnetic field turbulent amplitude. Each horizontal row of this histogram has been normalized to the maximum value of counts in that row. Figure 6b shows the number of counts (minutes of data with near- f_{ce} wave detections) included in each row. Figure 6c shows the number of counts (number of minutes) included in each column. The maximum possible number of wave detections per minute exceeds 60 because the cadence of the spectral data used to detect the waves is ~ 0.87 s (1 NYs).

For this figure, the amplitude of the magnetic field turbulence is estimated as follows: a Fourier transform was calculated for each component of the DC-coupled

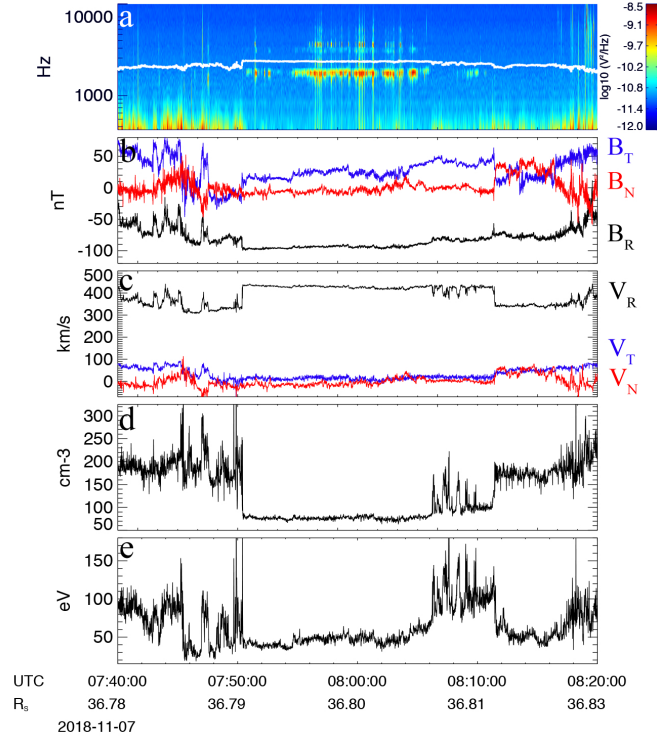


Figure 5. Example of near- f_{ce} waves in the near-Sun solar wind, with solar wind proton moments for context. (a) Spectrogram of the V_{12} differential voltage measurement. The thick white line indicates the local electron cyclotron frequency. (b) Ambient magnetic field vector in RTN coordinates. (c) Proton velocity in RTN coordinates. (d) proton density, (e) proton temperature.

magnetic field data within a minute-wide window. The three component power spectral densities were summed. The resulting spectra was flattened in frequency (f) space by dividing by $f^{-5/3}$. Finally, the average of the flattened power spectral density from 0.1 Hz to 1 Hz was calculated. This is the turbulence amplitude value on the x axis in Figure 6. A 1 Hz upper frequency cutoff is used to avoid the inclusion of ion cyclotron wave power (Bale & et al. 2019 (submitted)) and spacecraft-generated reaction wheel noise. The data in Figure 6 show a clear trend that near- f_{ce} waves are preferentially observed when the magnetic field turbulence is weak.

To gain insight into the origin of the instability that powers the near- f_{ce} waves, we examine the detection rate of near- f_{ce} waves as a function of electron core sunward

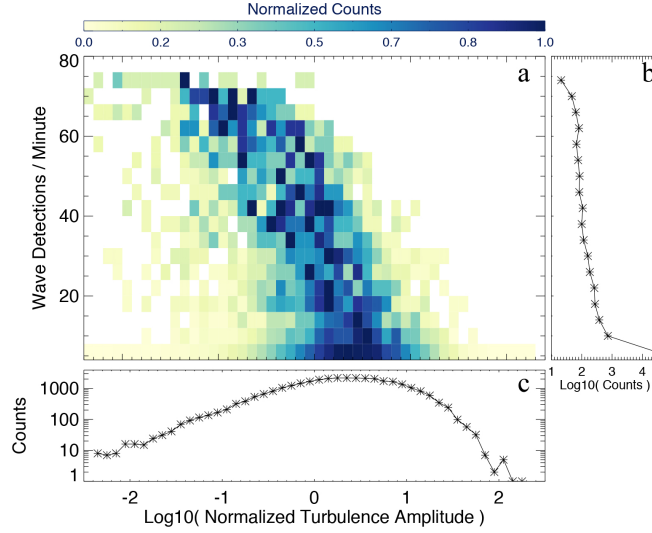


Figure 6. (a) Two-dimensional histogram showing the number of 1-minute data samples, normalized to the maximum value in each horizontal row, as a function of near- f_{ce} wave detections per minute and normalized magnetic field turbulence amplitude. (see text for explanations of the normalizations used). (b) The number of 1-minute data samples in each row of the histogram in (a). (c) The number of 1-minute data samples in each column of the histogram in (a).

drift, in the proton frame, measured by the SPANe electron instrument on Parker Solar Probe.

Figure 7 shows a two dimensional histogram in a similar format to Figure 6. For Figure 7a, the horizontal axis shows the electron core drift velocity averaged over 1 minute intervals. Positive values indicate magnetic field-aligned drift, negative values indicate anti-field-aligned drifts. Because the background magnetic field was oriented near-radial (approximately sunward during identified near- f_{ce} wave events) we interpret positive core drift velocities as sunward relative to the protons. Data from solar encounters 1 and 2 are included here. Again, Figures 7b and 7c show the number of data samples included in each horizontal row and vertical column (respectively). This analysis only includes electron distribution functions where the core could be fit (e.g. density detected by SPANe sufficiently high). For details on

the core fitting procedure and its limitations, see [Halekas & et al. \(2019 \(submitted\)\)](#) (this issue).

The core drift peaks near 100 km/s sunward for times when none or few near- f_{ce} waves are observed (bottom row of Figure 7a). As the number of waves detected per unit time increases, the core drift shifts toward 200 km/s, eventually reaching close to 300 km/s for the intervals with the most waves.

Near- f_{ce} waves are more frequently observed in regions where the electron core drift is more strongly sunward (in the frame of the solar wind protons). The sunward core drift velocity varies to balance the current associated with suprathermal electrons (strahl, halo) moving away from the Sun. Because the halo fractional density drops significantly during the solar encounters ([Halekas & et al. 2019 \(submitted\)](#) (this issue) and because the electron core and suprathermal currents nearly balance one another ([Halekas & et al. 2019 \(submitted\)](#) (this issue)), increases in the sunward core drift velocity indicate either: (i) regions where the strahl to core density increases, (ii) regions where the strahl velocity increases, or (iii) some combination of these. Core drift is used as a proxy for strahl measurements here because the near- f_{ce} waves are observed most often when the background magnetic field is near radial and the strahl distribution is often partially or largely blocked from the SPANe sensors by the Parker Solar Probe heat shield.

4. DISCUSSION

Near- f_{ce} waves are observed in regions where the ambient magnetic field is close to radial (Figure 2), magnetic turbulence is exceptionally weak (Figure 6), and the electron core sunward drift is enhanced (implying a larger suprathermal flux outward). Further, [Bale & et al. \(2019 \(submitted\)\)](#) reported that the near-Sun solar wind consists of ‘quiet’ radial-field intervals with weak turbulent fluctuations, punctuated by intervals of Alfvénic magnetic field reversals and strong magnetic field turbulence. Given these observations, and the understanding of whistler-mode wave growth de-

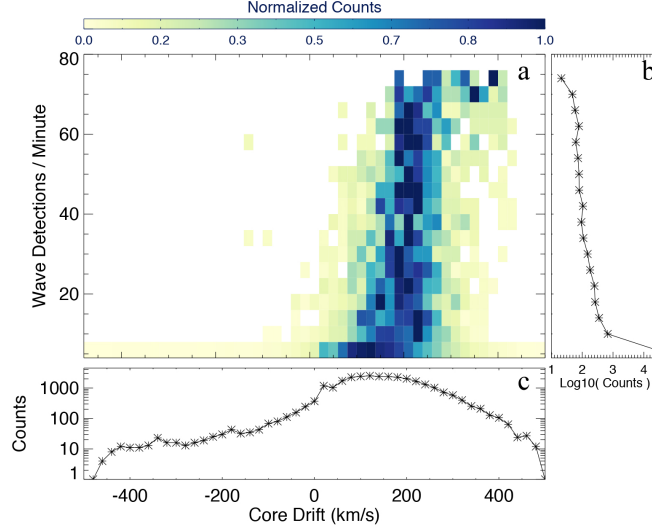


Figure 7. (a) Two-dimensional histogram showing the number of 1-minute data samples, normalized to the maximum value in each horizontal row, as a function of near- f_{ce} wave detections per minute and electron core drift velocity. (b) The number of 1-minute data samples in each row of the histogram in (a). (c) The number of 1-minute data samples in each column of the histogram in (a).

terminated from theory, simulation, and space measurements prior to Parker Solar Probe (Section 1), we postulate the following scenario for the origin of the near- f_{ce} waves.

Flux tubes where magnetic field turbulence is low contain a larger outward flux of strahl electrons. Those strahl electrons cause the sunward electron core drift (in the proton frame) to increase. The combination of larger strahl flux and more sunward electron core drift set up electron distribution functions unstable to near- f_{ce} wave growth. Details of the specific instability and wave growth process will be explored in future work.

The concept that the near-Sun solar wind is divided into 'quiet' magnetic flux tubes (where near- f_{ce} waves are preferentially observed) and 'strong turbulence' flux tubes where wave growth is suppressed is further supported by Figure 1 and Figure 5, where the bulk of near- f_{ce} wave power is observed in the center of each quiet, near-radial magnetic field region, rather than near the edges. Waves near the edges

would suggest growth due to instabilities associated with mixing plasma populations (e.g. (Malaspina et al. 2015; Holmes et al. 2018)). Waves near the magnetic structure center suggest that a property of the plasma within the flux tube is driving the instability.

However, this picture is incomplete. Why should flux tubes with 'quiet' solar wind (lower magnetic turbulence, hewing closer to the Parker spiral direction) show larger strahl electron flux? Perhaps this indicates multiple coronal source region properties. Perhaps it indicates different strahl radial evolution (efficiency of focusing and/or scattering) on 'quiet' versus 'strongly turbulent' magnetic flux tubes. Future work will explore these possibilities.

The preliminary identification of wave modes presented here (whistler / electron Bernstein) is based on wave frequency alone at this time. Future detailed study of polarization and other wave parameters may require that these initial identifications be reconsidered.

The correlation between near- f_{ce} waves and electron core drift in Figure 7 suggests that the waves are responding to changes in the local electron distribution function and supports the idea that the waves are generated close to where they are observed. However, given the low-turbulence, near-radial magnetic field configurations where the waves are observed, it is possible that the waves are generated closer to the Sun and propagate to the observing spacecraft. The efficiency of such a process could be enhanced if abrupt plasma density transitions at the boundaries of the low-turbulence, near-radial magnetic field regions (as in Figure 5) are common or persistent with radial distance from the Sun.

Finally, the observations presented here demonstrate that near- f_{ce} wave amplitude and occurrence in the data continue to increase toward the 35 R_S perihelion (Figure 4), suggesting that regions of quiet radial-field solar wind will become ever more common as Parker Solar Probe reduces its perihelion distance on future orbits.

5. CONCLUSIONS

We presented observations of plasma waves near the electron cyclotron frequency sunward of $50 R_S$. These waves have frequencies centered near $0.7 f_{ce}$ and f_{ce} , with strong harmonics. They are electrostatic up to the sensitivity of FIELDS. Their occurrence in the data and amplitude increase with decreasing distance to the Sun. They are observed during solar wind with near-radial magnetic field and weak magnetic field turbulence. A scenario for wave growth was postulated based on enhancements in strahl electron flux and corresponding electron core drift enhancements. Supporting evidence for this scenario based on electron observations was presented.

The study of near- f_{ce} waves in the near-Sun solar wind has only just begun, and already it promises to provide insight into the regulation of electron heat flux (through improved understanding of electron population evolution and its connection with wave growth), the large-scale structure of the solar wind (by implying flux tubes of weakly turbulent magnetic field stretching back toward the Sun), and the nature of kinetic wave-particle interactions in the near-Sun solar wind.

ACKNOWLEDGMENTS

The authors thank the Parker Solar Probe team, especially the FIELDS and SWEAP teams for their support. The FIELDS experiment on the Parker Solar Probe spacecraft was designed and developed under NASA contract NNN06AA01C. The authors wish to acknowledge helpful conversations with Dr. Ivan Vasko.

Facilities: Parker Solar Probe (FIELDS, SWEAP)

Software: SPEDAS ([Angelopoulos et al. 2019](#))

REFERENCES

- | | |
|---|---|
| <p>Angelopoulos, V., Cruce, P., Drozdov, A.,
et al. 2019, Space Science Reviews, 215,
9, doi: 10.1007/s11214-018-0576-4</p> | <p>Bale, S. D., & et al. 2019 (submitted),
Nature</p> |
|---|---|

- Bale, S. D., Goetz, K., Harvey, P. R., et al. 2016, *Space Science Reviews*, 204, 49, doi: [10.1007/s11214-016-0244-5](https://doi.org/10.1007/s11214-016-0244-5)
- Baumgaertel, K., & Sauer, K. 1989, *Journal of Geophysical Research*, 94, 11983, doi: [10.1029/JA094iA09p11983](https://doi.org/10.1029/JA094iA09p11983)
- Beinroth, H. J., & Neubauer, F. M. 1981, *J. Geophys. Res.*, 86, 7755, doi: [10.1029/JA086iA09p07755](https://doi.org/10.1029/JA086iA09p07755)
- Berčić, L., Maksimović, M., Landi, S., & Matteini, L. 2019, *MNRAS*, 486, 3404, doi: [10.1093/mnras/stz1007](https://doi.org/10.1093/mnras/stz1007)
- Breneman, A., Cattell, C., Schreiner, S., et al. 2010, *Journal of Geophysical Research (Space Physics)*, 115, A08104, doi: [10.1029/2009JA014920](https://doi.org/10.1029/2009JA014920)
- Bruno, R., & Carbone, V. 2013, *Living Reviews in Solar Physics*, 10, 2, doi: [10.12942/lrsp-2013-2](https://doi.org/10.12942/lrsp-2013-2)
- Feldman, W. C., Asbridge, J. R., Bame, S. J., Montgomery, M. D., & Gary, S. P. 1975, *Journal of Geophysical Research*, 80, 4181, doi: [10.1029/JA080i031p04181](https://doi.org/10.1029/JA080i031p04181)
- Fox, N. J., Velli, M. C., Bale, S. D., et al. 2016, *Space Science Reviews*, 204, 7, doi: [10.1007/s11214-015-0211-6](https://doi.org/10.1007/s11214-015-0211-6)
- Gary, S. P., Skoug, R. M., & Smith, C. W. 2005, *Physics of Plasmas*, 12, 056501, doi: [10.1063/1.1863192](https://doi.org/10.1063/1.1863192)
- Graham, G. A., Rae, I. J., Owen, C. J., et al. 2017, *Journal of Geophysical Research (Space Physics)*, 122, 3858, doi: [10.1002/2016JA023656](https://doi.org/10.1002/2016JA023656)
- Halekas, J. S., & et al. 2019 (submitted), *ApJ*
- Holmes, J. C., Ergun, R. E., Newman, D. L., et al. 2018, *Journal of Geophysical Research (Space Physics)*, 123, 9963, doi: [10.1029/2018JA025750](https://doi.org/10.1029/2018JA025750)
- Kajdič, P., Alexandrova, O., Maksimovic, M., Lacombe, C., & Fazakerley, A. N. 2016, *ApJ*, 833, 172, doi: [10.3847/1538-4357/833/2/172](https://doi.org/10.3847/1538-4357/833/2/172)
- Kasper, J. C., Abiad, R., Austin, G., et al. 2016, *Space Science Reviews*, 204, 131, doi: [10.1007/s11214-015-0206-3](https://doi.org/10.1007/s11214-015-0206-3)
- Lacombe, C., Alexandrova, O., Matteini, L., et al. 2014, *ApJ*, 796, 5, doi: [10.1088/0004-637X/796/1/5](https://doi.org/10.1088/0004-637X/796/1/5)
- Lengyel-Frey, D., Hess, R. A., MacDowall, R. J., et al. 1996, *Journal of Geophysical Research*, 101, 27555, doi: [10.1029/96JA00548](https://doi.org/10.1029/96JA00548)
- Lin, N., Kellogg, P. J., MacDowall, R. J., et al. 1998, *J. Geophys. Res.*, 103, 12023, doi: [10.1029/98JA00764](https://doi.org/10.1029/98JA00764)
- Maksimovic, M., Zouganelis, I., Chaufray, J. Y., et al. 2005, *Journal of Geophysical Research (Space Physics)*, 110, A09104, doi: [10.1029/2005JA011119](https://doi.org/10.1029/2005JA011119)
- Malaspina, D., Wygant, J., Ergun, R., et al. 2015, *Journal of Geophysical Research (Space Physics)*, 120, doi: [10.1002/2015JA021137](https://doi.org/10.1002/2015JA021137)
- Malaspina, D. M., Ergun, R. E., Bolton, M., et al. 2016, *Journal of Geophysical Research (Space Physics)*, 121, 5088, doi: [10.1002/2016JA022344](https://doi.org/10.1002/2016JA022344)
- Montgomery, M. D., Bame, S. J., & Hundhausen, A. J. 1968, *Journal of Geophysical Research*, 73, 4999, doi: [10.1029/JA073i015p04999](https://doi.org/10.1029/JA073i015p04999)
- Moullard, O., Burgess, D., Salem, C., et al. 2001, *Journal of Geophysical Research*, 106, 8301, doi: [10.1029/2000JA900144](https://doi.org/10.1029/2000JA900144)
- Narita, Y., Nakamura, R., Baumjohann, W., et al. 2016, *ApJL*, 827, L8, doi: [10.3847/2041-8205/827/1/L8](https://doi.org/10.3847/2041-8205/827/1/L8)
- Pilipp, W. G., Miggenrieder, H., Montgomery, M. D., et al. 1987, *Journal of Geophysical Research*, 92, 1075, doi: [10.1029/JA092iA02p01075](https://doi.org/10.1029/JA092iA02p01075)
- Ramírez Vélez, J. C., Blanco-Cano, X., Aguilar-Rodriguez, E., et al. 2012, *Journal of Geophysical Research (Space Physics)*, 117, A11103, doi: [10.1029/2012JA017573](https://doi.org/10.1029/2012JA017573)
- Saito, S., & Gary, S. P. 2007, *Geophys. Res. Lett.*, 34, L01102, doi: [10.1029/2006GL028173](https://doi.org/10.1029/2006GL028173)
- Seough, J., Nariyuki, Y., Yoon, P. H., & Saito, S. 2015, *ApJL*, 811, L7, doi: [10.1088/2041-8205/811/1/L7](https://doi.org/10.1088/2041-8205/811/1/L7)
- Shaaban, S. M., Lazar, M., Yoon, P. H., & Poedts, S. 2018, *Physics of Plasmas*, 25, 082105, doi: [10.1063/1.5042481](https://doi.org/10.1063/1.5042481)

- Stansby, D., Horbury, T. S., Chen, C. H. K., & Matteini, L. 2016, *ApJL*, 829, L16, doi: [10.3847/2041-8205/829/1/L16](https://doi.org/10.3847/2041-8205/829/1/L16)
- Tong, Y., Vasko, I. Y., Artemyev, A. V., Bale, S. D., & Mozer, F. S. 2019, *ApJ*, 878, 41, doi: [10.3847/1538-4357/ab1f05](https://doi.org/10.3847/1538-4357/ab1f05)
- Vocks, C., Salem, C., Lin, R. P., & Mann, G. 2005, *ApJ*, 627, 540, doi: [10.1086/430119](https://doi.org/10.1086/430119)
- Walsh, A. P., Arridge, C. S., Masters, A., et al. 2013, *Geophys. Res. Lett.*, 40, 2495, doi: [10.1002/grl.50529](https://doi.org/10.1002/grl.50529)
- Wilson, L. B., I., Cattell, C. A., Kellogg, P. J., et al. 2009, *Journal of Geophysical Research (Space Physics)*, 114, A10106, doi: [10.1029/2009JA014376](https://doi.org/10.1029/2009JA014376)
- . 2010, *Journal of Geophysical Research (Space Physics)*, 115, A12104, doi: [10.1029/2010JA015332](https://doi.org/10.1029/2010JA015332)
- Zhang, Y., Matsumoto, H., & Kojima, H. 1998, *J. Geophys. Res.*, 103, 20529, doi: [10.1029/98JA01371](https://doi.org/10.1029/98JA01371)